

# Topology-empowered membrane devices for terahertz photonics

Quanlong Yang<sup>a,b,\*</sup>, Dongyang Wang<sup>b,c</sup>, Sergey Kruk,<sup>a</sup> Mingkai Liu,<sup>a</sup> Ivan Kravchenko,<sup>d</sup> Jianguang Han,<sup>e</sup> Yuri Kivshar,<sup>a</sup> and Ilya Shadrivov<sup>a,\*</sup>

<sup>a</sup>Australian National University, Nonlinear Physics Centre, Research School of Physics, Canberra Acton, Australia

<sup>b</sup>Central South University, School of Physics and Electronics, Changsha, China

<sup>c</sup>The Hong Kong University of Science and Technology, Department of Physics, Hong Kong, China

<sup>d</sup>Center for Nanophase Materials Sciences, Oak Ridge National Laboratory, Oak Ridge, Tennessee, United States

<sup>e</sup>Tianjin University, Center for Terahertz Waves and College of Precision Instrument and Optoelectronics Engineering, Tianjin, China

**Abstract.** Control of terahertz waves offers a profound platform for next-generation sensing, imaging, and information communications. However, all conventional terahertz components and systems suffer from bulky design, sensitivity to imperfections, and transmission loss. We propose and experimentally demonstrate on-chip integration and miniaturization of topological devices, which may address many existing drawbacks of the terahertz technology. We design and fabricate topological devices based on valley-Hall photonic structures that can be employed for various integrated components of on-chip terahertz systems. We demonstrate valley-locked asymmetric energy flow and mode conversion with topological waveguide, multiport couplers, wave division, and whispering gallery mode resonators. Our devices are based on topological membrane metasurfaces, which are of great importance for developing on-chip photonics and bring many features into terahertz technology.

Keywords: topological devices; terahertz photonics; membrane; on-chip.

Received Mar. 22, 2022; revised manuscript received May 29, 2022; accepted for publication Jun. 13, 2022; published online Jul. 5, 2022.

© The Authors. Published by SPIE and CLP under a Creative Commons Attribution 4.0 International License. Distribution or reproduction of this work in whole or in part requires full attribution of the original publication, including its DOI.

[DOI: [10.1117/1.AP.4.4.046002](https://doi.org/10.1117/1.AP.4.4.046002)]

## 1 Introduction

Terahertz photonics is well known as a powerful and efficient tool for biosensing, nondestructive imaging, and detection of explosives.<sup>1,2</sup> More recently, due to ever-increasing demands for broadband wireless communications, the terahertz frequency range is considered to be a promising candidate for next-generation communication technologies, including 6G systems and beyond.<sup>3</sup> On-chip devices with dimensions much smaller than free-space counterparts attract considerable interest. However, existing terahertz devices are often bulky and lossy, and this limits their applicability in advanced technologies. The field of meta-optics offers pathways toward miniaturization and integration of photonic devices and systems.<sup>4,5</sup> The precise control of both electric and magnetic resonances enabled by meta-optics is vital for developing efficient and compact

electromagnetic components and devices.<sup>6–10</sup> Meta-devices based on free-standing dielectric membrane structure at the sub-wavelength scale are of particular practical importance as they remove many limitations associated with the negative impact of substrates on device performance.<sup>11–13</sup>

Importantly, terahertz devices can further be empowered by the physics of topological phases. Indeed, the recent discoveries of photonic topological insulators (PTIs) reveal that such materials may support robust edge states being immune to disorder and sharp bends.<sup>14–16</sup> Numerous theoretical predictions and experimental demonstrations have been made in a broad spectral range, from microwaves to visible, as well as for two-dimensional (2D) and three-dimensional (3D) systems.<sup>17–23</sup> Early approaches to the topological phases relied on an external magnetic field or a careful design, which has hindered widespread implementation. Meanwhile, great effort has been put into the study of valley-Hall photonics crystals (VHPCs), which support robust edge modes inside a photonic bandgap, but do not require time-reversal symmetry breaking.<sup>24–32</sup>

\*Address all correspondence to Quanlong Yang, [quanlong.yang@csu.edu.cn](mailto:quanlong.yang@csu.edu.cn); Ilya Shadrivov, [Ilya.Shadrivov@anu.edu.au](mailto:Ilya.Shadrivov@anu.edu.au)

For electromagnetic wave propagation, back-reflections are a major source of loss and feedback that hinders large-scale optical integration. While PTIs are strictly nonreciprocal and support one-way propagation, VHPCs are pseudospin-locked and support valley-polarized asymmetric propagation. The edge states of VHPCs propagate along the lattice interface, which provides a compact and reliable platform for on-chip integration.<sup>33,34</sup> The topologically protected edge states of VHPCs are robust against defects and exhibit near-unity transmission even through sharp corners. Hence, on-chip VHPCs show promise for robust, low-loss, and ultracompact waveguides, which are crucial for future THz integrated photonics.<sup>34</sup> In addition, these waveguides are single-mode and exhibit nearly ideal linear dispersion properties. As a result, there is a growing interest in bringing VHPCs to on-chip integration, however, the practical topological devices for integrated on-chip terahertz manipulation remain to be developed.

Here, we propose and realize experimentally several topology-empowered devices based on VHPCs of a perforated dielectric membrane for nontrivial on-chip terahertz wave manipulation. We demonstrate two types of domain walls separating rhombus lattices, where robust single-mode topological valley-polarized edge states are supported. In our experiment, in-plane electric field profiles of the topological waveguide are characterized with the terahertz near-field scanning system. In addition to the topological waveguide, we explore the topological multiport coupler, wave splitter, and whispering gallery mode (WGM) ring resonator based on two types of domain walls. The designed dielectric membrane devices present additional degrees of freedom for photonic topological state manipulation in comparison with conventional dielectric waveguides. Our study paves the way for the development of a robust and efficient platform for terahertz on-chip communication, sensing, and multiplexing systems.

## 2 Materials and Methods

### 2.1 Design of Topological Membrane Devices

Figure 1(a) illustrates the schematic design of topological membrane devices: low-index (air) circular hole pairs of radii of  $R_a$  and  $R_b$  are cut in a high-index (silicon) wafer with a permittivity of  $\epsilon = 11.7$ . The unit cells are arranged in a rhombus lattice with spacing  $a = 170 \mu\text{m}$  and the thickness of the suspended Si membrane is  $h = 90 \mu\text{m}$ . The lattice vectors are shown as  $a_1 = (a, 0)$  and  $a_2 = (a/2, \sqrt{3}a/2)$ . The radius difference of the two sublattice holes is denoted as  $\Delta = |R_a - R_b|$ . Here, we focus on the transverse-electric (TE)-like mode whose electric field lies predominantly in the  $x$ - $y$  plane. We conduct the eigenmode analysis of the periodic structure using the finite-element numerical method and extract the band diagram and field profiles as shown in Fig. 1(b). The simulation results were obtained  $10 \mu\text{m}$  above the upper surface of the topological devices and the discrete port is configured as a point dipole source and its polarization is confined in the  $x$ - $y$  plane. In the case with the inversion symmetry ( $R_a = R_b = 0.2a$ ), a degeneracy of the Dirac point ( $K$  valley) at 0.5 THz is shown by the dashed line in Fig. 1(b). By breaking the inversion symmetry ( $R_a = 0.25a$ ,  $R_b = 0.15a$ ), the Dirac point degeneracy is lifted in Fig. 1(b) (solid line), and a photonic bandgap opens from 0.46 to 0.54 THz (shaded region). The in-plane electric field magnitude profile and electric field vectors of the eigenmodes in the  $K$  valley are shown in the inset in Fig. 1(b). Two spin-polarized

transverse modes are found for the lower and upper bands, respectively, which correspond to the left-circular polarization (LCP) and right-circular polarization (RCP). Because they are not real spin polarizations, we denote these LCP or RCP-like edge modes as pseudospin modes.

The realization of VHPCs relies on the breaking of the inversion symmetry, and it features a nonvanishing Berry curvature accumulated around different valleys. At  $K$  or  $K'$  point, each valley displays a valley-Chern invariant of  $C_{k,k'} = \pm 1/2$  (see [Supplementary Material 1](#)). A domain wall formed between two parity-inverted VHPCs is topologically characterized by the mismatch of opposite valley-Chern numbers at a particular valley, which supports valley-polarized edge states within the optical bandgap. To study the edge states at the domain wall, we consider a waveguide configuration and numerically calculate the band diagram projection for a  $20 \times 1$  supercell. The results are shown in Fig. 1(c), where two edge modes show up in the projection bandgap, as indicated with red and blue curves, respectively. These two edge modes are found to be localized at the two types of domain walls DW1 [interface of  $(+\Delta, -\Delta)$  with larger holes adjacent to each other, edge mode in red curve] and DW2 [interface of  $(-\Delta, +\Delta)$  with smaller holes adjacent to each other, edge mode in blue curve] as shown in Figs. 1(d) and 1(e). In Fig. 1(c), we denote the  $K$  valley edge mode at DW1 (or  $K'$  at DW2) as  $\sigma+$ , and  $K'$  valley edge mode at DW1 (or  $K$  at DW2) as  $\sigma-$ , indicating the direction of group velocity. We note that for a particular domain wall, the edge modes at each valley have opposite group velocities, which indicates the valley-locked edge modes and asymmetric propagation in real space. The dispersion of edge states is single-mode and almost linear around the two valleys, which provides a uniform group velocity for achromatic propagation in the topological waveguide.

To confirm the edge mode dispersion properties, we performed the Fourier transformation of the in-plane electric field along the domain wall excited by a point dipole source. As displayed in Figs. 1(f) and 1(g), the in-plane electric field distributions are also calculated for two types of domain walls at 0.5 THz. Note that for the forward propagating wave at DW1, only the  $K$  valley is highlighted, which indicates that the excited edge state is  $K$  valley-locked (denoted as  $\sigma+$ ). Meanwhile, for the forward propagating mode along the DW2, it is  $K'$  valley-locked (also denoted as  $\sigma+$ ), which shows an inverse valley-polarization compared to DW1.

### 2.2 Experimental Verification of Topological Waveguide

To experimentally demonstrate the transmission signature and electric field profile of VHPCs, we fabricated the topological waveguide starting with a silicon-on-insulator wafer and using photolithography and deep reactive ion etching techniques (see [Supplementary Material 2](#)). Figures 2(a) and 2(b) display the optical and SEM image of the fabricated samples with DW1, and the white dashed line denotes the position of the interface that acts as the topological waveguide. This topological waveguide supports two counterpropagating edge modes with different valley-polarizations; for simplicity, only the forward propagating ( $\sigma+$ , along the positive  $x$ -direction) edge mode is considered here. Figure 2(c) shows the calculated transmission spectra of the topological waveguide (solid line), where an electric dipole placed on the surface of the membrane is used to excite the edge state in the simulation. A distinct transmission window from 0.46 to 0.54 THz can be clearly seen from the

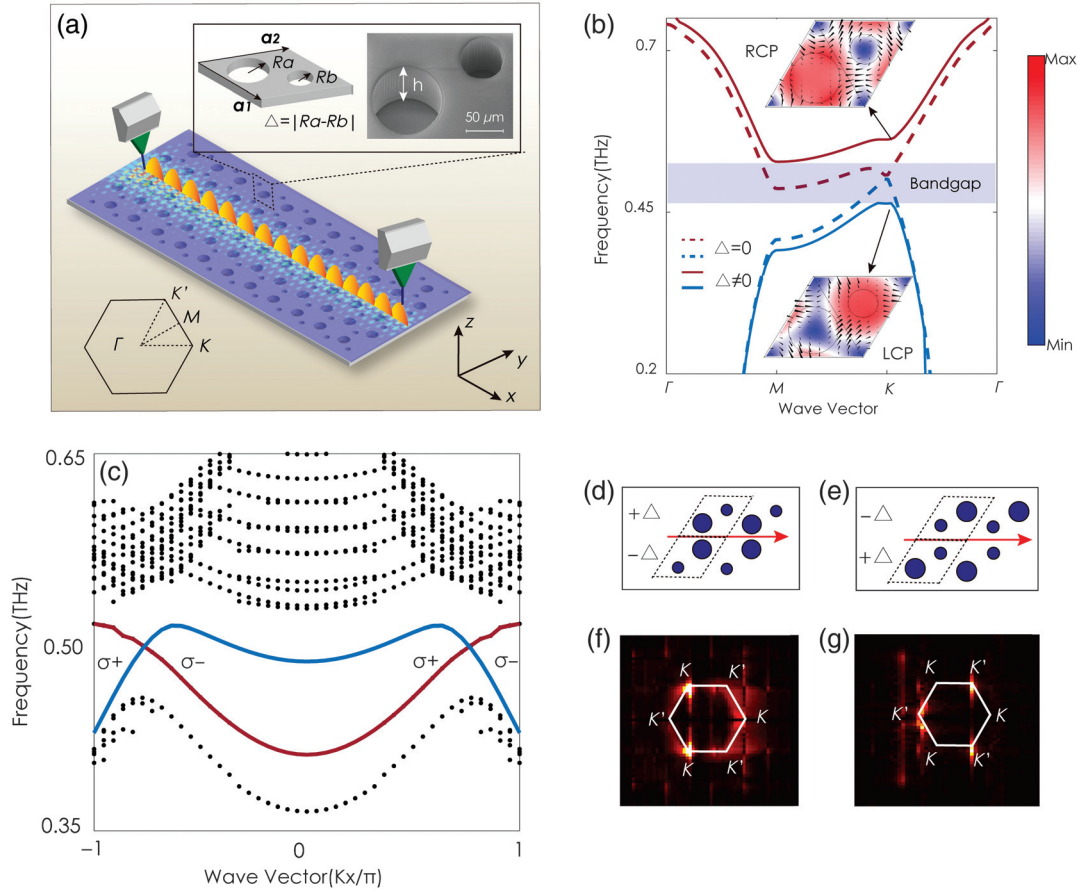


**Fig. 1** Concept of topological membrane meta-devices. (a) Schematic of topological membrane meta-devices and terahertz near-field scanning microscope systems. Two terahertz probes are employed as the emitter and detector to map the in-plane field distributions of the topological meta-devices. The inset shows the schematic view and the electron microscope image of the fabricated unit cell of the VHPCs. (b) Photonic band structure of meta-atoms with (dashed line) and without (solid line) inversion symmetry,  $\Delta = |R_a - R_b|$  is the radius difference between the two circular holes. The inset shows the mode profiles of meta-atoms in the  $K$  valley, and the arrows denote the electric field vectors. (c) Calculated dispersion of topological edge states from a  $20 \times 1$  supercell, data points in black are projection bands. (d), (e) Schematic of the two studied domain walls (DW1 and DW2). The  $\Delta$  is of the opposite sign for the two sides of the domain walls, as is also seen as a mirror arrangement of holes across the interface. DW1 and DW2 are denoted as  $(+\Delta, -\Delta)$  and  $(-\Delta, +\Delta)$ , respectively. (f), (g) Fourier spectra of DW1 and DW2 at 0.5 THz were obtained from the calculated real space electric field distribution.

normalized transmission spectra for all the  $E_x$ ,  $E_y$ , and  $H_z$  field components.

In the experiment, a broadband fiber-based terahertz near-field spectroscopy system is employed to characterize the performance of the topological membrane devices. Two terahertz probes are used as the transmitter and detector, respectively. The emitter that serves as a dipole source is mounted on a 3D motorized translation stage that enables 2D scans at a fixed distance from the sample surface. The tilt angle of the probe is set to 30 deg to get the best coupling efficiency to the topological waveguide. The optical image of the terahertz emitter and detector is shown in Fig. 2(a). The employed system includes a near-field excitation source and a near-field detection probe (Protomics GmbH). Such a configuration allows us to selectively excite individual waveguides and map field distributions around them. The measured transmission spectra are shown in

Fig. 2(c) as the dashed line for the  $E_y$  field component and it is in good agreement with the calculated results. We attribute the small discrepancy between the experiment and the calculated results to the fabrication imperfections and strong dependency of the measured signal on the exact position of the detector. When positioning the near-field antennas with a finite precision, the amplitude of the electric field varies significantly with the probe position above the sample due to the exponential decay of the edge mode along the  $y$  direction shown in Fig. 2(g).

In Figs. 2(d) and 2(e), we show the in-plane electric field ( $E_x, E_y$ ) profile from simulation for 0.5 THz, where the TE-like field profile is presented. The edge modes are excited by the dipole source placed near the left edge of the sample and propagate along the  $x$  direction, the field is confined to the straight waveguide, and it penetrates into each side of the domain wall by approximately five periods ( $850 \mu\text{m}$ ). Figure 2(f) shows the

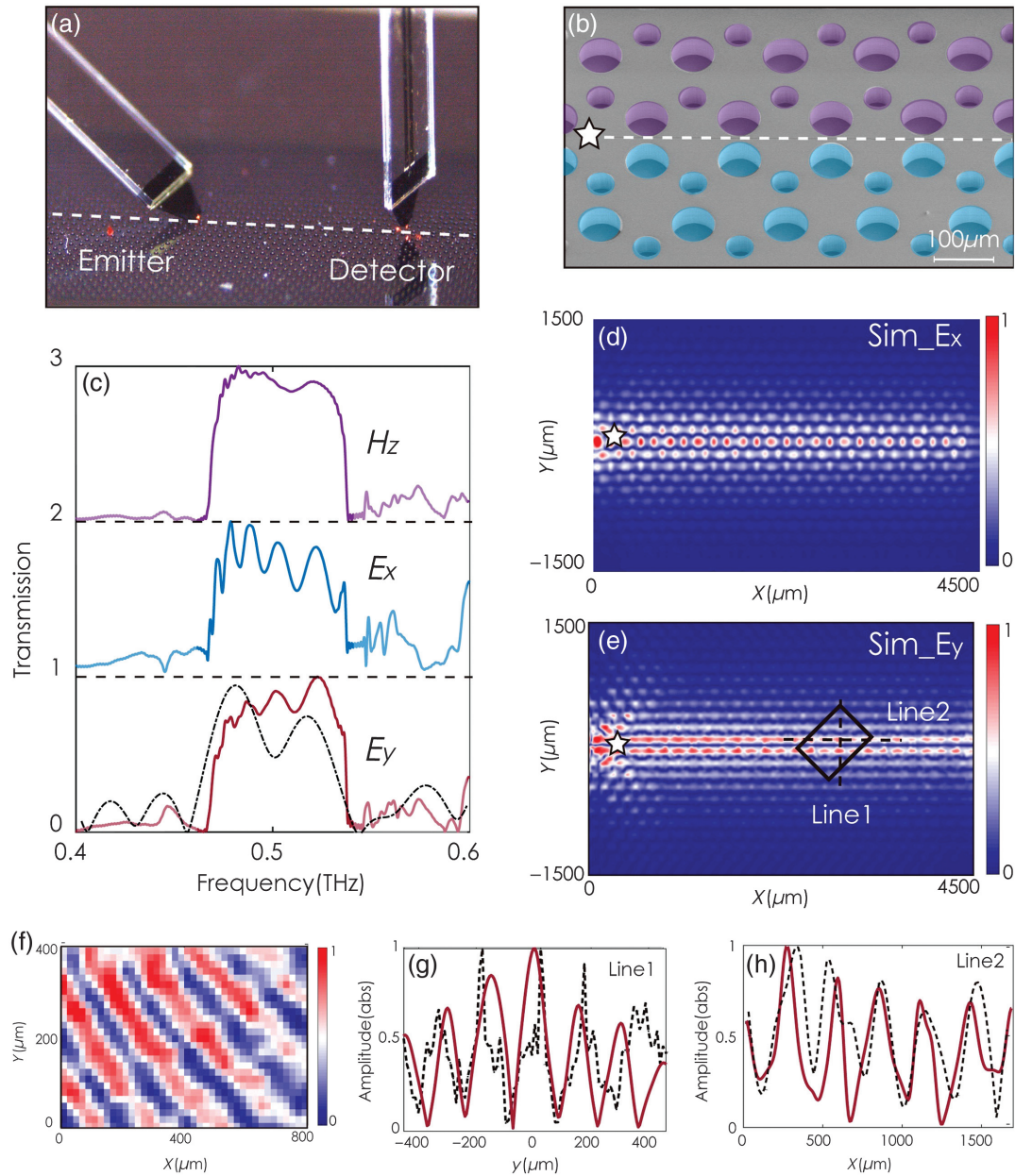


**Fig. 2** Topological on-chip waveguides. (a) Optical image of the terahertz near-field microscope probes and the fabricated topological waveguide. The white dashed line denotes the position of the topological waveguide as DW1. (b) SEM image of the fabricated straight waveguide with two parity-inverted VHPCs lattices. (c) Calculated (solid line) and measured (dashed line) transmission curves of  $E_x$ ,  $E_y$ , and  $H_z$  for the topological waveguide. (d), (e) Calculated in-plane electric field magnitude distribution for the topological waveguide at 0.5 THz. The white star denotes the position of the excitation source. (f) Measured  $E_y$  field distributions of the topological waveguide marked by the black rectangle in (e). (g), (h) Calculated (red solid line) and measured (black dashed line) 1D  $E_y$  field distributions across and along the waveguide [lines 1 and 2 in (e)], respectively.

experimentally measured  $E_y$  component of the electric field, and a rectangular region marked by the black rectangle in Fig. 2(e) is selected for the detailed experimental scan. The measured field in Fig. 2(f) demonstrates a good agreement with the simulation results. Due to the limitations of the THz near-field microscope, we are not able to measure the field distribution over the whole device. To show the good agreement of simulated and measured

results, we present one-dimensional (1D) electric field profiles across the waveguide and along the waveguide [lines 1 and 2 in Fig. 2(e)] and plot them in Figs. 2(g) and 2(h). The measured field profile of the  $E_y$  component is in good agreement with the calculated results in Fig. 2(e), which demonstrated the interface confinement and exponential decay of the edge states. Here, the calculated decay lengths for simulation and experiment results

are 810 and 780  $\mu\text{m}$ , respectively. Further calculations are discussed in [Supplementary Material 3](#).

### 3 Results

#### 3.1 Topological Couplers

To demonstrate the capability of terahertz on-chip devices based on VHPCs, we studied topological multiport couplers. Due to the availability of the two types of domain walls, there are multiple combinations that can be used for constructing couplers, and we consider several of them. The surface modes at the domain

walls are valley-locked as indicated in Fig. 3(a), and this prohibits the intervalley scattering on a fixed domain wall and thus supports the possibility of building various directional couplers. Due to the inverted configuration of DW1 and DW2, the  $K(K')$  valley of DW1 is equivalent to the  $K'(K)$  valley for DW2. For convenience, we denote the surface modes at the  $K$  valley of DW1 and the  $K'$  valley of DW2 as  $\sigma+$ , while the surface mode at the  $K'$  valley of DW1 and the  $K$  valley of DW2 as  $\sigma-$ . The valley locking of surface states can thus be recognized as a conservation of pseudospin  $\sigma$ , i.e.,  $\sigma+$  ( $\sigma-$ ) can only scatter into  $\sigma+$  ( $\sigma-$ ).

We first consider a configuration of the multiport couplers shown in Figs. 3(b) and 3(c), where DW1 and DW2 form sharp

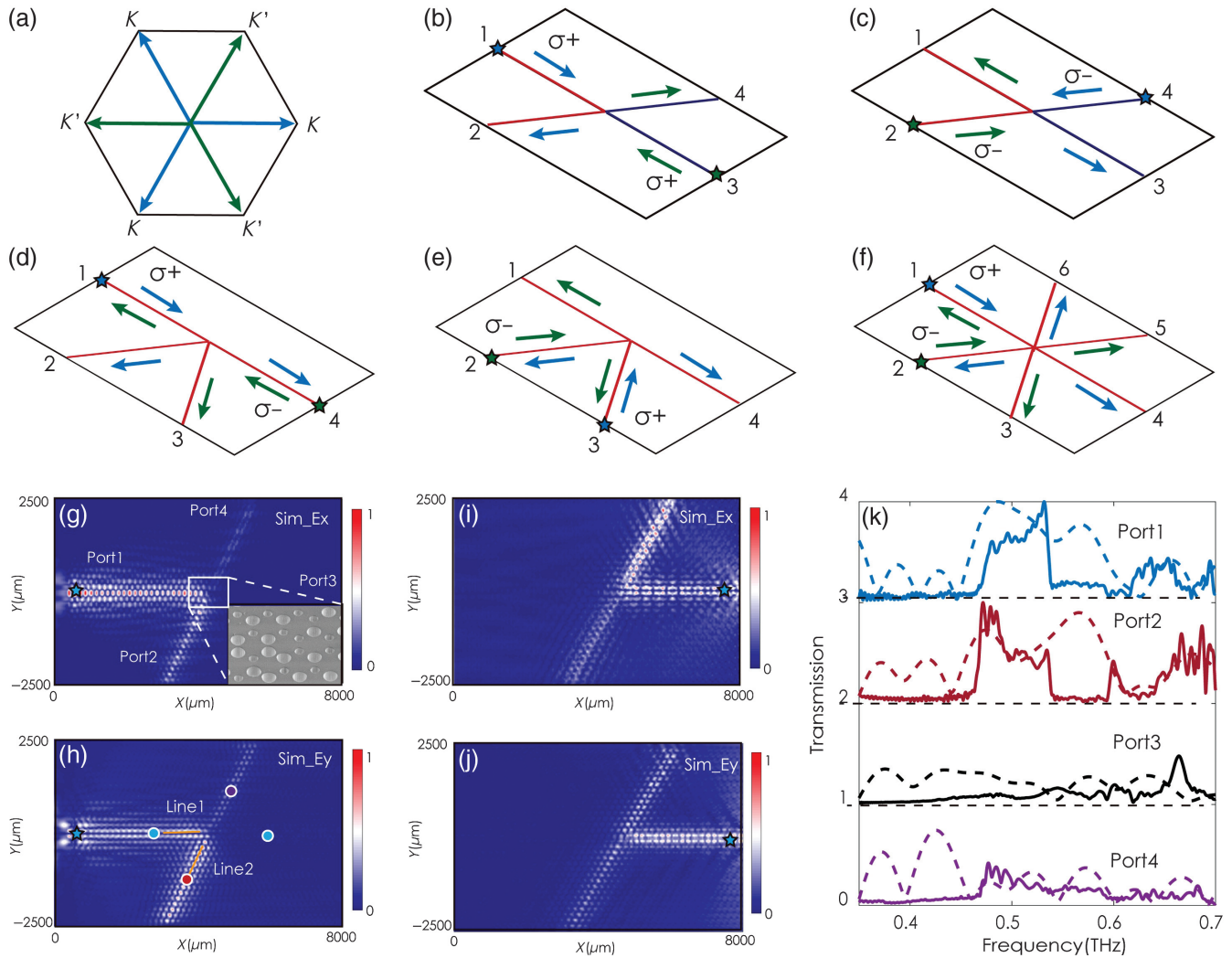


**Fig. 3** Topological on-chip multiport couplers. (a) Valley-locked surface modes at domain walls. The blue and green arrows denote the surface mode at the  $K$  and  $K'$  valley, respectively. (b), (c) Schematic of the four-port directional coupler consisting of DW1 (red) and DW2 (navy). The arrows denote the power flow of two edge states at the  $K$  and  $K'$  valley, and the stars indicate the excitation source. (d)–(f) Conceptual illustration of the topological directional coupler with four identical DW1 and six-port coupler consisting of six identical DW1. (g), (h) Calculated in-plane field distribution ( $E_x$  and  $E_y$ ) on the topological four-port coupler at 0.5 THz with the source at port 1. The inset is the SEM image of the junction point. (i), (j) Corresponding calculated in-plane field distribution with the source at port 3. (k) Calculated and measured transmission of four different ports with the excitation from port 1. Each measurement is taken 10 unit cells from the junction so that the measurement at port 1 corresponds to the incident wave. The signal detection positions are shown by colored circles in (h).

bends and join at the center of the devices (DW1 and DW2 are marked by red and navy lines, respectively). For this topological four-port coupler, the supported propagation directions of the  $\sigma+$  surface mode are illustrated in Fig. 3(b). Port 1 with DW1 only supports the forward propagation of the  $\sigma+$  edge state ( $K$  valley, blue arrow). Therefore, when the four-port coupler is excited from port 1, the edge state  $\sigma+$  propagates to the junction point. Due to the mismatch of the pseudospin, there is no transmission of energy to port 3. Both ports 2 and 4 support the coupling of the edge mode  $\sigma+$ , but the structure of the field distribution at the junction point and mode overlap between the waveguides determine the coupling efficiencies for these two ports. Only a small fraction of energy is allowed to couple into port 4, and port 2 receives most of the energy. These predictions agree well with the calculated electric field profiles ( $E_y$ ) of the four-port coupler at 0.5 THz, as shown in Fig. 3(g). Because the  $E_x$  component of the four-port couplers shows a similar conclusion, we did not show it here for simplification. To further characterize the propagation of other edge states along with four ports, the calculated electric field profiles with the source placed in ports 2, 3, and 4 are presented in Figs. 3(h)–3(j). When we excite other ports, the behavior of the coupler in these cases shares the same features as the first case shown in Fig. 3(g), which is in good agreement with the prediction.

We fabricate the four-port coupler as displayed in the inset of Fig. 3(g), where the SEM image of the junction point is shown. The measurement of four ports is taken 10 unit cells away from the junction point, which is marked by the points in Fig. 3(h) with different colors. The measured transmission for four ports is shown in Fig. 3(k), where ports 1 and 2 display distinct transmission windows indicating the presence of edge modes within the bandgap (100% and 67% at 0.5 THz). Port 3 displays close to zero transmission (4.5%), and there is a fraction of energy that goes into port 4 (23%) as expected. There is only an  $\sim 5.5\%$  transmission loss after the mode passes sharp corners, which demonstrates the robustness and topological imperfections of our topological devices. Moreover, the 1D electric field profiles show a similarity to the measured results for the topological waveguide in Fig. 2(g); see [Supplementary Material 4](#) for further details.

We introduce another topological four-port coupler that is formed by only the DW1 type waveguide, as shown in Figs. 3(d) and 3(e). This coupler works as a traditional directional coupler. When the source is located at port 1, only the edge state  $\sigma+$  is excited and the wave propagates toward ports 2 and 4, while nothing reaches port 3 due to the principle of pseudospin conservation. On the other hand, when excited from port 4 (green color), the energy is coupled to ports 1 and 3. Excitation from ports 2 and 3 is shown in Fig. 3(e), where the reverse operation of the directional coupler can be seen. More excitation configurations and the demonstration of the valley-locked directional coupling can be found in [Supplementary Material 5](#). Furthermore, the schematic of the topological six-port coupler consisting of six identical DW1 is shown in Fig. 3(f), which is equivalent to a combination of two directional couplers in Figs. 3(d) and 3(e). Like the earlier analysis of the directional coupler, we find that there are four ports that support the valley-locked edge state with  $\sigma+$  or  $\sigma-$ . For example, port 1 to ports 2, 4, 6 for  $\sigma+$  and port 2 to port 1, 3, 5 for  $\sigma-$ . The demonstration of the performance of the topological six-port couplers is presented in [Supplementary Material 6](#).

### 3.2 Topological Splitter

Next, we demonstrate the topological beam splitter shown in Fig. 4. Figure 4(a) shows the schematic of the proposed topological beam splitter. Three DW1 (red line) and three DW2 (navy line) are used in this device. When the splitter is excited from port 1, the forward propagating edge state  $\sigma+$  is coupled into ports 2 and 3 with the ratio of 50:50. We show the calculated 2D electric field profile of the topological beam splitter at 0.5 THz in Fig. 4(b), where the  $E_y$  field components at ports 2 and 3 are evenly distributed. Zero transmission is found for port 4. We also fabricated the topological beam splitter; the corresponding optical and SEM images of the fabricated sample are shown in Figs. 4(d) and 4(e).

In Figs. 4(c) and 4(f), we show the frequency dependency of the fabricated beam splitter with both the simulation and experimental results. We note that the experimental curve appears to be smoother than the calculated one since the frequency resolution of our spectrometer is not sufficient for confirming all the fine features seen in the simulations. The transmission is studied at points marked in Fig. 4(b) with different colors, and we can see in Fig. 4(c) that the edge mode of port 1 (whose energy we take as 100% at 0.5 THz) is split into ports 2 and 3 with equal amplitudes (48.3%). A close to zero transmission in port 4 (0.7%) and a 2.7% transmission loss from the junction point are also observed, which demonstrates the robustness and topological imperfections of our topological design. The measured transmission for four ports is displayed in Fig. 4(f), and it shows a good agreement with calculated results. Here, if we assume the measured signal in port 1 at 0.5 THz as 100%, then ports 2 and 3 receive 44.75% and 40%, respectively. Considering the loss from the junction and the bends, the signal splitting in the device is still close to 50%. Moreover, by extending this beam splitter with its mirror image, we can construct a topological Mach–Zehnder interferometer, which can be employed for on-chip sensing and phase-sensitive measurements. Further discussion is presented in [Supplementary Material 7](#).

### 3.3 Topological Ring Resonator

The optical ring resonators offering an enhanced light-matter interaction are appealing for many applications ranging from biosensing to quantum optical devices as well as integrated on-chip systems.<sup>35–37</sup> Topological photonics was used to create ring resonators;<sup>38–42</sup> however, we perform the first demonstrations in the terahertz frequency range. To explore potential on-chip devices based on the valley-locked edge states, we implement a topological membrane ring resonator based on the WGM, as illustrated in Fig. 5. For the conventional WGM resonator shown in Fig. 5(a), both the waveguide and the ring support the forward and backward propagating modes. When the straight waveguide is excited at the frequencies not matching the resonant frequency of the WGMs, there will be near-zero coupling between the waveguide and the ring. When the frequencies match, the energy flows into the ring resonator and affects the transmission of the wave through the waveguide. The forward and backward couplings between the ring and the waveguide are both supported.

By alternately arranging DW1 and DW2, we built a topological hexagonal WGM resonator, which supports clockwise propagation of  $\sigma+$  and counterclockwise propagation of  $\sigma-$ . The propagation of edge modes at the hexagonal ring complies with the same mechanism of multiport couplers in Fig. 3(a), and

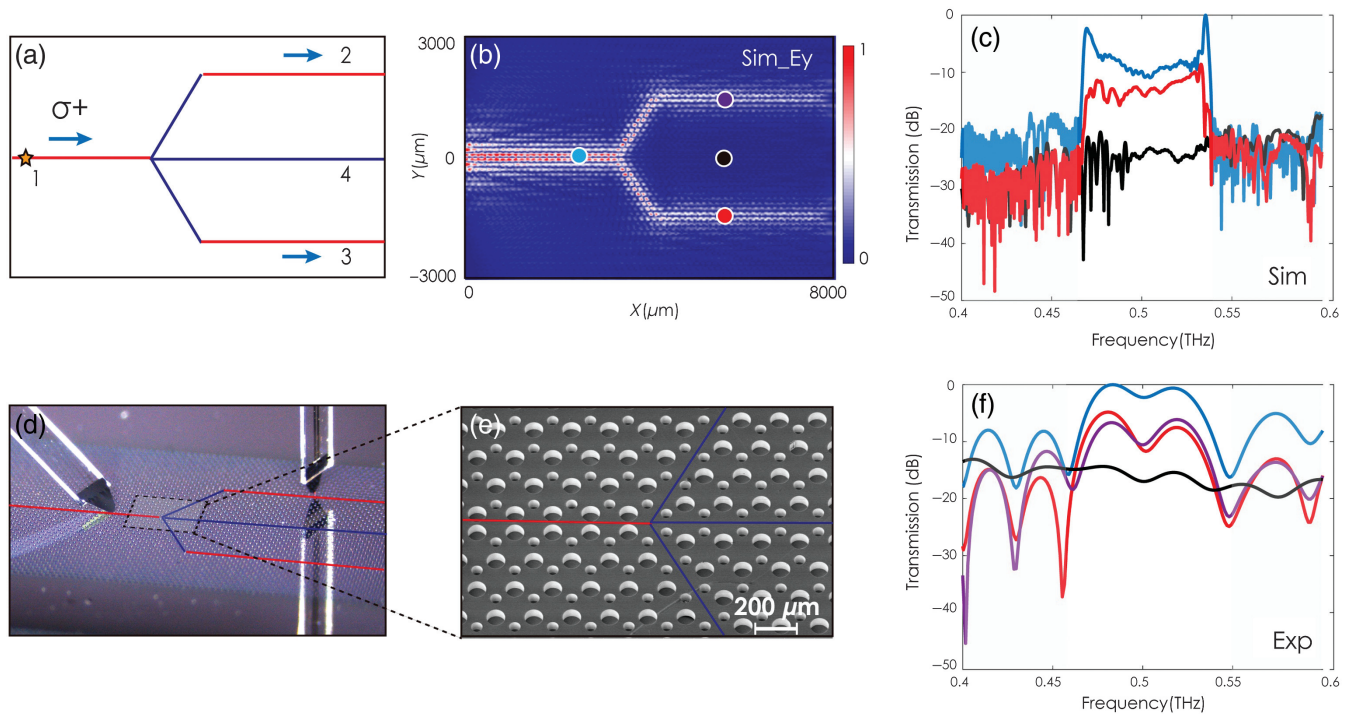


**Fig. 4** Topological on-chip splitters. (a) Schematic of the topological splitter containing DW1 (red line) and DW2 (navy line) waveguides. The blue and green arrows denote the power flow of the two edge states  $\sigma+$  and  $\sigma-$ . (b) Calculated in-plane electric field distribution on the topological splitter at 0.5 THz. (c), (f) Calculated and experimentally measured transmission spectra for in-plane components at positions 1 to 4. The signal detection positions are shown in (b). (d), (e) Optical image of the fabricated topological beam splitter placed in the terahertz near-field microscope. The inset shows the SEM image of the junction point.

there is very small reflection at the bends. In Fig. 5(b), we show a coupling of the waveguide mode to the topological hexagonal WGM resonator, when the waveguide away from the resonator is excited. Away from the resonant frequencies, the behavior of the topological resonator is like the conventional WGM resonator except for the suppression of the backward propagating mode ( $\times$  of backward modes). For the resonator shown in Fig. 5(b), there is only the counterclockwise propagating mode  $\sigma+$  that is allowed to couple to the waveguide. As to the coupling output, modes in the ring resonators due to pseudospin matching only support the coupling to the forward mode ( $\checkmark$ ). More interestingly, when the critical coupling is satisfied, no edge state on the ring could couple forward, and the energy is trapped within the ring ( $\times$  of forward modes as dashed arrow).

Simulation results for the resonances of the topological WGM resonator are shown in Figs. 5(d) and 5(e), where the spacing between the resonator and the waveguide is equal to five periods (see Supplementary Material 9). In Fig. 5(d), we excite from the waveguide and calculate the electric field at two points shown in the figure: blue is on the ring, and red is on the waveguide. There are three main resonance peaks 2 to 4 (0.518, 0.523, and 0.528 THz, the resonance frequency positions depend on the circumference of the ring) on the rings and three transmission dips in the waveguide field spectrum, which indicate that the energy is coupled to the ring. In particular, the transmission for 0.528 THz drops to near zero, which corresponds to the critical coupling regime. We show the mode

structure for these discrete frequencies in Fig. 5(e). The simulation results show that no electric field couples to the ring at 0.5 THz, as the wave propagates along the straight waveguide. Due to the strong coupling at 0.518 and 0.523 THz, the power flows into the ring resonator and obvious traveling wave patterns are observed in the ring. As for coupling output, only the forward modes are supported, as indicated by “ $\checkmark$ ” in the schematic in Fig. 5(b), and their direction is shown by the white arrow in Fig. 5(e). Moreover, the edge modes at 0.528 THz display a zero transmission, and we can see that all the energy is trapped in the ring and the electric field profile shows a standing wave pattern. Due to the limited frequency resolution of our current near-field time-domain spectroscopy, we were not able to detect these high- $Q$  resonances in the experiment.

We also study a different configuration when we excite the topological WGM resonator directly, as shown in Fig. 5(c). Since we use the point dipole source, the edge modes with different propagation directions ( $\sigma+$ , counterclockwise, and  $\sigma-$  for clockwise) are both excited. The outcoupling from the ring to the waveguide is found in two situations. It is worth mentioning that the edge states  $\sigma+$  and  $\sigma-$  couple to the waveguide in opposite directions. Figure 5(f) illustrates the fields in the resonator and waveguide when the resonator is excited directly. In comparison to the case of the waveguide excitation, due to the coupling limitation between the waveguide and ring, the excitation of the ring directly shows a larger number of WGMs. The electric field profiles of the edge states at four discrete

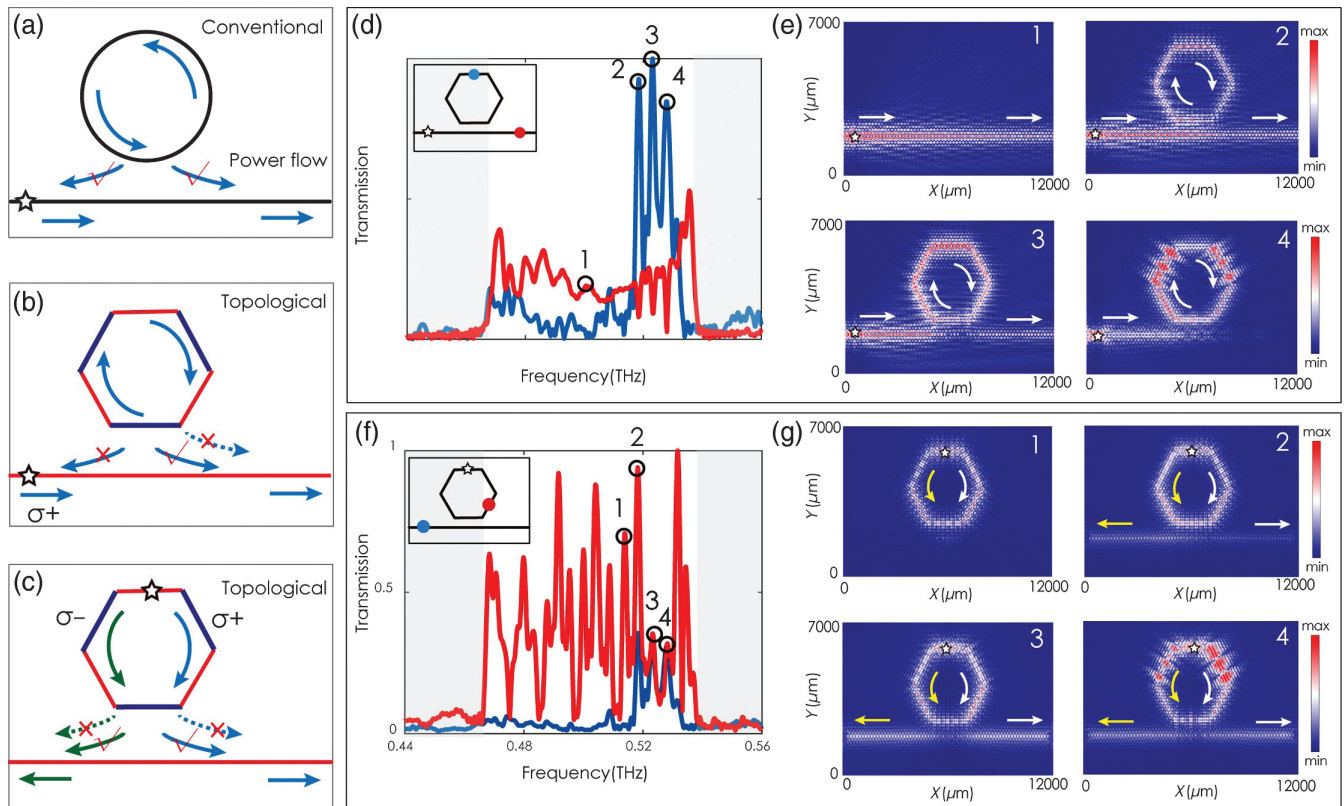


**Fig. 5** Topological on-chip resonators. (a) Mode coupling of a conventional whispering gallery mode resonator. The arrows show the direction of possible power flow, while stars indicate the position of the excitation source. The energy from the ring couples into both the forward and backward propagating modes of the waveguide. (b) Mode conversion of topological resonators with the source located in the waveguide. The arrows denote the supported ( $\checkmark$ ) and forbidden ( $\times$ ) directions of coupling, and red and navy lines denote DW1 and DW2, respectively. Two types of resonances (traveling and standing waves) arise depending on the coupling of the forward propagation. The dashed arrow denotes the critical coupling. (c) Corresponding mode conversion of topological resonators with the source located on the ring. (d) Electric field spectrum in the resonator (measured at the location of the blue point shown in the inset) and the straight waveguide (red point). (e)  $E_y$  field distributions of the topological resonators at peaks 1 to 4 (0.5, 0.518, 0.523, and 0.528 THz). The white arrows denote the power flow of the edge modes  $\sigma+$ . (f), (g) Corresponding electric field spectrum and field distributions of four peaks 1 to 4 (0.513, 0.518, 0.523, and 0.528 THz) with the source exciting the ring directly. The white and yellow arrows display the power flow of the edge modes  $\sigma+$  and  $\sigma-$ , respectively.

frequencies are shown in the right panel of Fig. 5(g), where opposite outcoupling to the waveguide can be seen.

## 4 Conclusion

We have designed and demonstrated experimentally several terahertz topological devices based on valley-Hall photonics for integrated on-chip systems. Valley-locked edge modes at discrete domain walls are utilized for mode coupling and conversion. The employment of a terahertz near-field spectroscopy system allows us to directly characterize and visualize the valley-locked edge states on our proposed topological devices, including the waveguide, directional couplers, and beam splitters. We also studied the coupling of topological waveguides to topological ring resonators and observed selective coupling defined by the mode pseudospin. This demonstration opens an avenue toward terahertz topological on-chip photonic networks for

next-generation wireless communications, biosensing, and quantum computing.

## Acknowledgments

The work was supported by the Australian Research Council (Grant Nos. DP200101168 and DP210101292). Development of manufacturing technology and actual production of terahertz topological devices were conducted as part of a user project at the Center for Nanophase Materials Sciences (CNMS), at the US Department of Energy, Office of Science User Facility at Oak Ridge National Laboratory. The authors declare no competing financial interests.

## Code, Data, and Materials Availability

The data that support the findings of this study are available from the corresponding author upon reasonable request.

## References

1. R. Singh et al., "Ultrasensitive terahertz sensing with high- $Q$  Fano resonances in metasurfaces," *Appl. Phys. Lett.* **105**(17), 171101 (2014).
2. D. M. Mittleman, "Twenty years of terahertz imaging," *Opt. Express* **26**(8), 9417–9431 (2018).
3. H. Srieddeen et al., "Next generation terahertz communications: a rendezvous of sensing, imaging, and localization," *IEEE Commun. Mag.* **58**(5), 69–75 (2020).
4. N. I. Zheludev and Y. S. Kivshar, "From metamaterials to meta-devices," *Nat. Mater.* **11**(11), 917–924 (2012).
5. S. B. Glybovski et al., "Metasurfaces: from microwaves to visible," *Phys. Rep.* **634**, 1–72 (2016).
6. N. Yu et al., "Light propagation with phase discontinuities: generalized laws of reflection and refraction," *Science* **334**(6054), 333–337 (2011).
7. Y. Yang et al., "All-dielectric metasurface analogue of electromagnetically induced transparency," *Nat. Commun.* **5**, 5753 (2014).
8. S. Wang et al., "Broadband achromatic optical metasurface devices," *Nat. Commun.* **8**, 187 (2017).
9. S. Kruk and Y. Kivshar, "Functional meta-optics and nanophotonics governed by mie resonances," *ACS Photonics* **4**(11), 2638–2649 (2017).
10. S. Sun et al., "Electromagnetic metasurfaces: physics and applications," *Adv. Opt. Photonics* **11**(2), 380–479 (2019).
11. J. R. Ong et al., "Freestanding dielectric nanohole array metasurface for mid-infrared wavelength applications," *Opt. Lett.* **42**(13), 2639–2642 (2017).
12. Q. Yang et al., "Mie-resonant membrane Huygens' metasurfaces," *Adv. Func. Mater.* **30**(4), 1906851 (2020).
13. Q. Yang et al., "Polarization-sensitive dielectric membrane metasurfaces," *Adv. Opt. Mater.* **8**(20), 2000555 (2020).
14. A. B. Khanikaev et al., "Photonic topological insulators," *Nat. Mater.* **12**(3), 233–239 (2013).
15. L. Lu et al., "Topological photonics," *Nat. Photonics* **8**(11), 821–829 (2014).
16. A. B. Khanikaev and G. Shvets, "Two-dimensional topological photonics," *Nat. Photonics* **11**(12), 763–773 (2017).
17. M. C. Rechtsman et al., "Photonic Floquet topological insulators," *Nature* **496**(7444), 196–200 (2013).
18. M. Hafezi et al., "Imaging topological edge states in silicon photonics," *Nat. Photonics* **7**(12), 1001–1005 (2013).
19. A. Blanco-Redondo et al., "Topological protection of biphoton states," *Science* **362**(6414), 568–571 (2018).
20. S. Barik et al., "A topological quantum optics interface," *Science* **359**(6376), 666–668 (2018).
21. Y. Yang et al., "Realization of a three-dimensional photonic topological insulator," *Nature* **565**(7741), 622–626 (2019).
22. D. Smirnova et al., "Third-harmonic generation in photonic topological metasurfaces," *Phys. Rev. Lett.* **123**(10), 103901 (2019).
23. D. Wang et al., "Photonic Weyl points due to broken time-reversal symmetry in magnetized semiconductor," *Nat. Phys.* **15**(11), 1150–1155 (2019).
24. J.-W. Dong et al., "Valley photonic crystals for control of spin and topology," *Nat. Mater.* **16**(3), 298–302 (2017).
25. J. Noh et al., "Observation of photonic topological valley Hall edge states," *Phys. Rev. Lett.* **120**(6), 063902 (2018).
26. F. Gao et al., "Topologically protected refraction of robust kink states in valley photonic crystals," *Nat. Phys.* **14**(2), 140–144 (2018).
27. M. I. Shalaev et al., "Robust topologically protected transport in photonic crystals at telecommunication wavelengths," *Nat. Nanotechnol.* **14**(1), 31–34 (2019).
28. M. Wang et al., "Valley-locked waveguide transport in acoustic heterostructures," *Nat. Commun.* **11**, 3000 (2020).
29. S. Arora et al., "Direct quantification of topological protection in symmetry-protected photonic edge states at telecom wavelengths," *Light Sci. Appl.* **10**(1), 9 (2021).
30. M. T. A. Khan et al., "3D-printed terahertz topological waveguides," arXiv:2010.16299 (2020).
31. T. Ma and G. Shvets, "All-Si valley-Hall photonic topological insulator," *New J. Phys.* **18**(2), 025012 (2016).
32. H. Xue et al., "Topological valley photonics: physics and device applications," *Adv. Photonics Res.* **2**, 2100013 (2021).
33. J. Cha et al., "Experimental realization of on-chip topological nanoelectromechanical metamaterials," *Nature* **564**(7735), 229–233 (2018).
34. Y. Yang et al., "Terahertz topological photonics for on-chip communication," *Nat. Photonics* **14**(7), 446–451 (2020).
35. Y. Yang and Z. H. Hang, "Topological whispering gallery modes in two-dimensional photonic crystal cavities," *Opt. Express* **26**(16), 21235–21241 (2018).
36. C. Wang et al., "Electromagnetically induced transparency at a chiral exceptional point," *Nat. Phys.* **16**(3), 334–340 (2020).
37. S.-Y. Yu et al., "Critical couplings in topological-insulator waveguide-resonator systems observed in elastic waves," *Nat. Sci. Rev.* **8**(2), nwa262 (2021).
38. M. A. Bandres et al., "Topological insulator laser: experiments," *Science* **359**(6381), eaar4005 (2018).
39. M. Jalali Mehrabad et al., "Chiral topological photonics with an embedded quantum emitter," *Optica* **7**(12), 1690–1696 (2020).
40. G. Q. Liang and Y. D. Chong, "Optical resonator analog of a two-dimensional topological insulator," *Phys. Rev. Lett.* **110**(20), 203904 (2013).
41. Q. Lin et al., "A three-dimensional photonic topological insulator using a two-dimensional ring resonator lattice with a synthetic frequency dimension," *Sci. Adv.* **4**(10), 2774 (2018).
42. L. Gu et al., "A topological photonic ring-resonator for on-chip channel filters," *J. Lightwave Technol.* **39**(15), 5069–5073 (2021).

**Quanlong Yang** obtained his PhD from Tianjin University in 2018. He was a postdoctoral research fellow of the Australian National University from 2019 to 2022. He is currently an associate professor at Central South University. His research interests are in terahertz science and technology, all-dielectric metasurfaces, topological photonics, and nonlinear photonics.

**Ilya Shadrivov** obtained his PhD from the Australian National University in 2005. He is currently a Professor at the Research School of Physics of the Australian National University. His interests include nonlinear optics, metamaterials and metasurfaces, photonic crystals, novel microwave devices, terahertz wave manipulation and physics of disordered structures.

Biographies of the other authors are not available.